

1 **Impacts of Elevated Dissolved CO₂ on a Shallow Groundwater System:**

2 **Reactive Transport Modeling of a Controlled-Release Field Test**

3 Liange Zheng^a, Nicolas Spycher^a, Marco Bianchi^b, John D. Pugh^c, Charuleka
4 Varadharajan^a, Ruth M. Tinnacher^a, Jens T. Birkholzer^a, Peter Nico^a and Robert C.
5 Trautz^d
6

7 ^a *Lawrence Berkeley National Laboratory, Berkeley, California 94720, USA*

8 ^b *British Geological Survey, Kingsley Dunham Centre, Keyworth, Nottingham, NG12*
9 *5GG, UK*

10 ^c *Southern Company Services, 600 N. 18th St., Birmingham, Alabama 35291, USA*

11 ^d *Electric Power Research Institute, 3420 Hillview Avenue, Palo Alto, California 94304,*
12 *USA*

13

14 **Abstract**

15 One of the risks that CO₂ geological sequestration imposes on the environment is the
16 impact of potential CO₂/brine leakage on shallow groundwater. The reliability of reactive
17 transport models predicting the response of groundwater to CO₂ leakage depends on a
18 thorough understanding of the relevant chemical processes and key parameters affecting
19 dissolved CO₂ transport and reaction. Such understanding can be provided by targeted
20 field tests integrated with reactive transport modeling. A controlled-release field
21 experiment was conducted in Mississippi to study the CO₂-induced geochemical changes
22 in a shallow sandy aquifer at about 50m depth. The field test involved a dipole system in
23 which the groundwater was pumped from one well, saturated with CO₂ at the pressure
24 corresponding to the hydraulic pressure of the aquifer, and then re-injected into the same
25 aquifer using a second well. Groundwater samples were collected for chemical analyses
26 from four monitoring wells before, during and after the dissolved CO₂ was injected. In

27 this paper, we present reactive transport models used to interpret the observed changes in
28 metal concentrations in these groundwater samples. A reasonable agreement between
29 simulated and measured concentrations indicates that the chemical response in the aquifer
30 can be interpreted using a conceptual model that encompasses two main features: (a) a
31 fast-reacting but limited pool of reactive minerals that responds quickly to changes in pH
32 and causes a pulse-like concentration change, and (b) a slow-reacting but essentially
33 unlimited mineral pool that yields rising metal concentrations upon decreased
34 groundwater velocities after pumping and injection stopped. During the injection, calcite
35 dissolution and Ca-driven cation exchange reactions contribute to a sharp pulse in
36 concentrations of Ca, Ba, Mg, Mn, K, Li, Na and Sr, whereas desorption reactions control
37 a similar increase in Fe concentrations. After the injection and pumping stops and the
38 groundwater flow rate decreases, the dissolution of relatively slow reacting minerals such
39 as plagioclase drives the rising concentrations of alkali and alkaline earth metals observed
40 at later stages of the test, whereas the dissolution of amorphous iron sulfide causes slowly
41 increasing Fe concentrations.

42

43 **1. Introduction**

44

45 Ever since the concept of CO₂ geologic storage was proposed about two decades ago,
46 many studies have been undertaken to assess hydrological, geochemical and mechanical
47 processes affecting deep injection and containment of CO₂ in storage reservoirs.
48 Meanwhile, as part of environmental risk assessments for CO₂ storage sites, studies have
49 also been undertaken to assess the impacts of potential CO₂ leaks from deep storage

50 reservoirs, on the quality of overlying fresh water aquifers (see review papers by
51 Lemieux, 2011 and Harvey et al., 2012, and references therein). Numerical modeling has
52 been an important tool to address this issue.

53 Reactive transport models were first used to evaluate the potential impacts of CO₂
54 leakage on the water quality of shallow, overlying aquifers (Wang and Jaffe, 2004;
55 Carroll et al., 2009; Zheng et al., 2009; Apps et al., 2010; Wilkin and Digiulio, 2010), and
56 to identify potential issues such as the leaching out of organics such as BETX, PAH,
57 from source rocks (Zheng et al., 2013; Zhong et al., 2014). Later on, they were used to
58 interpret data from laboratory experiments (e.g. Viswanathan et al., 2012; Zheng et al.,
59 2016) and field tests (e.g. Zheng et al., 2012; Trautz et al., 2013 and Zheng et al., 2015)
60 in order to understand key physical and chemical processes that control the response of
61 aquifers to CO₂ leakage. Most recently, reactive transport models have been used to
62 predict potential long-term change in aquifer in response to CO₂/brine leakage (Bacon et
63 al., 2016), to conduct uncertainty quantifications (Hou et al., 2014) to lay the foundation
64 for risk assessment studies, and to provide guidance for risk management and mitigation.

65 Laboratory experiments provide useful information on the type and quantity of
66 trace elements that may be mobilized in response to CO₂ intrusion into potable
67 groundwater, forming the basis for further modeling analyses. Such experiments (Smyth
68 et al., 2009; Lu et al., 2010; Little and Jackson, 2010, Wei et al., 2011; Viswanathan et al.,
69 2012; Humez et al., 2013; Varadharajana et al., 2013; Wunsch et al., 2014; Kirsch et al.,
70 2014; Lawter et al., 2016) were typically conducted in batch or column mode, where CO₂
71 was released into a pre-equilibrated water-rock environment and the geochemical
72 changes in the aqueous phases were monitored subsequently. Modest to strong increases

73 in concentrations of major and trace elements have typically been reported in these
74 laboratory experiments, although in terms of the changes of one particular element,
75 different experiments have led to different results. For example, increases in Fe
76 concentration has been reported in Smyth et al. (2009) and Lu et al. (2010), whereas
77 Humez et al. (2013) observed declining Fe concentrations after initial CO₂ influx. The
78 increase or decrease in metal concentrations also varies significantly from one
79 experiment to another, likely due to differences in experimental conditions, types of
80 sediments, mineralogical compositions, etc. However, despite these differences, one
81 common observation is a concentration increase for alkali and alkaline earth metals and
82 Si.

83 Laboratory experiments have some inherent limitations such as (1) failing to
84 preserve the *in situ* water-rock environment as a result of pre-equilibration of sediments
85 with a synthetic solution (e.g., Smyth et al., 2009) or DI water (Lu et al., 2010), (2)
86 unwanted oxidation of sediments samples during the experiment (e.g., Little and Jackson,
87 2010), or (3) the failure to include transport of groundwater and CO₂. Several field tests
88 have been conducted to further enhance our understanding of potential impacts of CO₂
89 leakage on shallow groundwater. The ZERT (Zero Emissions Research and Technology)
90 field test in Montana, USA (Kharaka et al., 2010; Spangler et al., 2010) was probably the
91 first controlled-release experiment in this regard, with food-grade CO₂ injected over a 30
92 day period into a horizontal perforated pipe a few feet below the water table of a shallow
93 aquifer. Cahill and Jakobsen (2013) and Cahill et al. (2014) reported a field scale pilot
94 test in which CO₂ gas was injected at 5-10 m depth into an unconfined aquifer in
95 Denmark for two days, and water geochemistry changes were monitored for more than

96 100 days. As reported in Peter et al. (2012), CO₂ was injected through 3 wells for a
97 period of 10 days into an aquifer at 18 m depth in Northeast Germany. All these tests
98 involved an injection of CO₂ or CO₂-bearing water into the aquifer, and the monitoring of
99 changes in water composition via monitoring wells downstream of the injection point. In
100 general, observations made in field tests are largely consistent with those from laboratory
101 tests in terms of concentration increases for major and trace elements, but there are two
102 noticeable differences: first, the level of concentration changes observed in the field is
103 typically much lower than in the laboratory. For example, an increase in major and trace
104 element concentrations of 1 to 3 orders of magnitude has been observed in the laboratory
105 compared to field tests, which never show an increase greater than one order of
106 magnitude (i.e., 20% to 700%). Secondly, concentration increases in trace elements,
107 especially for elements of environmental concern such as As, Pb, Ba, Cd, are more
108 frequently observed in laboratory than in field tests.

109 A thorough understanding of key physical and chemical processes and related parameters
110 is critical for building a reliable model to predict long term changes in aquifer response to
111 CO₂/brine leakage. Researchers have postulated based on laboratory-scale experimental
112 results (e.g. Lu et al., 2010), the simulation of laboratory-scale data (e.g. Humez et al.,
113 2011; Viswanathan et al., 2012; Zheng et al., 2015b) or field tests (e.g. Zheng et al.,
114 2012; Trautz et al., 2013) that a number of chemical processes are potentially responsible
115 for the mobilization of trace elements. These include the dissolution of carbonates (e.g.,
116 Kharakha et al., 2006; McGrath et al., 2007; Lu et al., 2010), sulfides (e.g., Wang and
117 Jaffe, 2004; Zheng et al., 2009; Apps et al., 2010) and iron oxyhydroxide minerals (e.g.,
118 Kharaka et al., 2006, 2009), as well as surface reactions such as adsorption/desorption

119 (Viswanathan et al., 2012) and ion exchange (Kharaka et al., 2006, 2009; Zheng et al.,
120 2009; Apps et al., 2010; Zheng et al., 2012; Cahill et al., 2014). The degree to which
121 these reactions contribute to water quality impacts depends on the specific aqueous
122 chemistry and aquifer mineralogy for a given system. Field testing integrated with
123 reactive transport modeling provides an effective and reliable way to identify reactions
124 and parameters that are needed to build reliable simulation tools for risk assessments of
125 CO₂ sequestration.

126 A comprehensive longer-term field study involving the controlled release of
127 groundwater containing dissolved CO₂ was initiated in 2011 to investigate potential
128 groundwater impacts in Mississippi, USA (Trautz et al., 2013). Injection of dissolved
129 CO₂ lasted approximately 5 months followed by an extended phase of post-injection
130 groundwater monitoring. The experiment involved extensive laboratory and field
131 characterization of groundwater and sediments, an innovative fluid-delivery system,
132 hydrologic monitoring, and geophysical monitoring for remote detection of dissolved
133 CO₂. Trautz et al. (2013) presented the data from this test at one of the monitoring wells,
134 including preliminary results of reactive transport simulations, and Varadharajan et al.
135 (2013) reported laboratory test results for aquifer sediments collected while drilling wells
136 for this test. In this paper, we present reactive transport simulations conducted to
137 interpret groundwater monitoring data at the site over a significantly longer time frame
138 than initially reported by Trautz et al. (2013), with the goal to elucidate key chemical
139 processes and parameters that could affect observed changes in long-term dissolved metal
140 concentrations in groundwater at this test site.

141

142 **2. Field test**

143 **2.1. Test description**

144 The study site is located in Jackson County Mississippi and lies in the Pascagoula River
145 Drainage Basin in the Gulf Coastal Plain physiographic province, which is
146 topographically gently rolling to flat with local salt marshes. The stratigraphic interval
147 into which carbonated water was injected is composed of fine silty sand with minor clay
148 interbedding at depths between 46.9 and 54.6 m (Figure 1, right). An innovative closed
149 loop groundwater delivery system was used to pump groundwater from the confined
150 shallow aquifer through a carbonation unit to infuse it with CO₂ before injecting the
151 carbonated groundwater back into the same shallow aquifer. The test configuration is
152 shown in Figure 1: groundwater is injected through well IW-1 and pumped out from well
153 PW-1. Groundwater samples were collected from the five monitoring wells over three
154 test periods (Table 1): (1) for 13 months prior to pumping and injection (background), (2)
155 for five months during pumping and injection, and (3) for 10 months after pumping and
156 injection ended. Groundwater samples were analyzed in the laboratory to evaluate trends
157 in major and minor cations, anions, trace elements, organic carbon, and dissolved gases.
158 In addition, geophysical monitoring using complex electrical tomography allowed
159 changes in electrical resistivity of the groundwater to be observed, and the position of the
160 dissolved CO₂ plume as it migrated between wells to be tracked (Dafflon et al., 2013).

161 Table 1. Test period durations

Test Period	Start Date	End Date	Approx. Duration	Wells Sampled
--------------------	-------------------	-----------------	-----------------------------	--------------------------

			(months)	
Pre-CO ₂ injection baseline	2-Sep-2010	18-Oct-2011	13	All wells
Pre-pumping (static baseline)	2-Sep-2010	12-Aug-2011	11	All wells
Pumping (dynamic baseline)	12-Aug-2011	18-Oct-2011	2	MW, BG wells
CO ₂ injection (pumping continues)	18-Oct-2011	23-Mar-2012	5	MW, BG wells
Post-CO ₂ injection	23-Mar-2012	15-Jan-2013	10	MW, BG wells

162

163 A decrease in groundwater pH by 1.5–3 units was observed at nearby monitoring
164 wells as the dissolved CO₂ plume migrated through the sandy aquifer. In general, four
165 groups of metals exhibiting different trends in metal/solute concentration changes (with
166 limited exceptions) were observed during the test: (1) solutes below
167 detection/background concentration levels (Type I: Al, Sb, As, Be, Cd, Cu, Pb, Hg, Ag,
168 Tl, Zn, P, Se, Br⁻, Cl⁻, NO₂⁻, NO₃⁻, SO₄²⁻, HS⁻), (2) metals potentially leaching out of
169 geophysical probes employed in the field experiment (Type II: Cr, Co Ni), (3) metals
170 displaying an apparent concentration increase upon injection of CO₂ (Type III: Ba, Ca, Fe,
171 Li, Mg, Mn, K, Si, Na, and Sr) and (4) those showing a concentration decrease (Type IV:
172 Mo and F) after exposure to dissolved CO₂. It should be noted that none of the metal
173 concentrations measured during the controlled release experiment exceeded primary
174 drinking water standards (i.e., maximum contaminant levels) established by the U.S.
175 Environmental Protection Agency under the Clean Water Act.

176

177 **2.2. Trend analyses of observed metal concentrations**

178 In previous work, we reported on the early-time groundwater composition trends
179 observed during the first few months after injection of carbonated water started (Trautz et
180 al., 2013). For several metals (Ba, Ca, Fe, Li, Mg, Mn, K, Si, Na, Sr), the concentration
181 data exhibited a clear “pulse”-like response (see Figure 2 for Sr as example) upon arrival
182 of carbonated groundwater at the monitoring well closest to the injection point (MW-3).
183 This response was attributed to Ca-driven exchange reactions triggered by the dissolution
184 of a very small, finite amount of calcite in the sediments. As groundwater quality data
185 continued to be collected over a longer time frame, it became evident that the
186 concentration of some metals (e.g., Ca, Ba, Fe) started to slowly increase once pumping
187 and injection ended and the groundwater velocities returned to ambient conditions
188 (Zheng et al., 2015). This later increase (superposed on an initial fast, exchange-driven
189 pulse) was attributed to slow mineral dissolution, noticeable only under conditions of
190 increased groundwater residence time once the pump was turned off (Zheng et al., 2015).

191 Here, we further evaluate the groundwater quality response to carbonation using
192 the *full* set of analytical data collected *before* (13 months), *during* (5 months), and *after*
193 the release of CO₂ (10 months after turning off the injection pump). Accordingly, the
194 monitoring data were classified into three groups: *pre-*, *during*, and *post*-injection, with
195 the ‘*pre*-injection’ data defined as analyses before the arrival of the carbonated plume at
196 specific wells, measured as the start of the pH decrease at these wells. Thus, these data
197 may include samples that were technically sampled during the injection period but prior
198 to plume arrival.

199 Using these three sets of data together, elemental correlation plots (Figure 3) and
200 Principal Component Analyses (PCA; Figure 4; Numerical Dynamics, 2014), including
201 multivariate regression were performed to further distinguish trends and possible
202 differences in responses to carbonation. Metal concentration data collected prior to
203 injection ('pre' in Figure 3) show a narrow variability with regards to a correlation to Ca
204 concentrations. During CO₂ injection, the strongest correlation between Ca and other
205 released metals is observed for Ba, Mg, Sr, and Mn (Figure 3). These metals were shown
206 to have significantly higher concentrations in pH-5 sequential leachates of sediments
207 collected from the field site (Varadharajan et al., 2013). Post-pumping data for these
208 elements exhibit more scattered and possibly different correlation trends (Figure 3),
209 which would support the hypothesis of the two distinct release mechanisms (during and
210 post-pumping, respectively) postulated by Zheng et al. (2015). Similar analyses also
211 show some correlation of Ca with Fe, Na, and alkalinity, as well as a good correlation
212 between Fe and Mn. A weaker correlation of Si with Ca (Figure 3) (and also Na, not
213 shown) although quite more scattered, also lends support to the hypothesis of Zheng et al.
214 (2015) suggesting that the slow dissolution of plagioclase may contribute to the long-term
215 concentration trends of these elements.

216 Plots of PCA loadings allow for an evaluation of the similarity or dissimilarity of
217 measured dissolved metal concentrations. Points located in close proximity have a
218 common denominator, thus in our case, possibly a similar metal source and/or release
219 mechanism. The PCA loadings for individual elements (Figure 4) show three groups of
220 metal correlations. First, elements falling in the upper left quadrant of Figure 4 (Ba, Ca,
221 Co, Li, Mg, Mn, Na, Si, and Sr) include seven of the top ten loadings contributors; these

222 correspond to metals that were shown to yield high concentrations in acid leachates of
223 site sediments (Varadharajan et al., 2013). The consistent grouping of these elements in
224 both the field and laboratory studies confirms that these elements form a distinct group of
225 released metals. Second, Fe, Cr, and Ni appear to form their own group (lower left
226 quadrant in Figure 4), suggesting another source and/or release mechanism for these
227 elements in the field study. No release was observed for these metals in leaching
228 experiments (Varadharajan et al., 2013). One possible explanation is a contamination of
229 groundwater samples with corrosion products from stainless steel geophysical electrodes
230 that were deployed in the field but not present in lab-scale experiments. Third, alkalinity,
231 chloride, and dissolved organic matter also fall within the top 10 contributors, but in this
232 case because of their individual variability, or lack thereof.

233 **2.3. Postulated metal release mechanisms**

234 The release of trace elements from sediments due to reaction with dissolved CO₂
235 has been explained by various mechanisms including: (1) the dissolution of calcite with
236 trace amounts of impurities of other elements (Lu et al., 2010), (2) metal desorption from
237 mineral surfaces (Viswanathan et al., 2012; Zheng et al., 2012), (3) the dissolution of
238 silicate minerals (Yang et al., 2013), and/or (4) cation exchange reactions, which are
239 triggered by an increase in Ca⁺² concentrations after calcite dissolution (Zheng et al.,
240 2012). To date, metal concentration trends observed in most tests reported in the
241 literature have been monotonic increases, mainly because laboratory tests were typically
242 performed in batch experiments—without any transport component—and most field tests
243 were conducted over fairly short time periods (Kharaka et al., 2010). One exception is a
244 field test in which CO₂ gas was injected into a shallow aquifer at 5-10 m depth for 72

245 days, followed by post-injection monitoring of the groundwater composition (Cahill et al.,
 246 2014). During this test, concentrations of major and trace elements increased first upon
 247 arrival of the carbonated groundwater, but then decreased during the remaining CO₂
 248 injection period, and continued to decrease over the post injection time-period. In contrast,
 249 during the field test conducted for the present study, a rapid pulse-like release of
 250 dissolved cations upon the arrival of carbonated groundwater was observed, followed by
 251 slowly-rising cation concentrations almost immediately after the injection was stopped.

252 This latter behavior can be explained by a conceptual model that includes two
 253 contaminant release source terms (Zheng et al., 2015): (a) a fast-reacting but limited pool
 254 of reactive minerals that responds quickly to changes in pH, and (b) a slow-reacting but
 255 essentially unlimited mineral pool that yields slowly rising concentrations upon decreased
 256 groundwater velocities (increased residence time) after pumping and injection stopped.
 257 The fast-reacting and slow-reacting pools, and the associated release processes, are
 258 believed to differ for different elements, as summarized in Table 2 and discussed in
 259 further detail below. The geochemical models developed in this study were set up to
 260 simulate the minerals (pools) and processes postulated in this table.

261

262 Table 2. Fast-reacting, limited and slow-reacting, unlimited pools proposed for
 263 the release of Type III metals.

Element	Fast-reacting limited pool	Slow-reacting unlimited pool
Ca	Calcite dissolution	Plagioclase (Ab ₈₀ An ₂₀) dissolution

Ba, Mg, Mn, K, Li, Na, Sr	Cation exchange with Ca	No specific minerals. However, Ca from the slow-reacting Ca pool (plagioclase) triggers further cation exchange with these metals.
Fe	Desorption	Iron sulfide (FeS _m) dissolution
Si	Desorption	Plagioclase (Ab ₈₀ An ₂₀) dissolution

264

265

266 3. Groundwater Flow and Geochemical Model Development

267 The reactive transport models in this paper focus on the Type (III) metals/metalloids
 268 discussed earlier, because the increasing dissolved concentration of these metals upon
 269 exposure to CO₂-saturated water is obviously of more potential concern than the
 270 decreasing or un-detectable concentrations of the other metals. The simulations were
 271 conducted with TOUGHREACT V2 (Xu et al., 2011), a numerical model that was
 272 developed by introducing reactive chemistry into the existing framework of a non-
 273 isothermal multi-phase multi-component fluid and heat flow simulator, TOUGH (Pruess
 274 et al., 1999).

275

276 3.1. Model domain and discretization

277 Because the aquifer was found to be fairly homogeneous in the vertical direction,
 278 a 2-D planar (X-Y) model was employed. The spatial domain of the groundwater flow
 279 covers an area of about 500 m × 500 m. An area of 40 m × 100 m was finely discretized
 280 with a 1-m grid size. Areas of 20 m × 40 m surrounding the injection well and monitoring
 281 wells have even finer gridding with a 0.5-m grid size (Figure 5). A honeycomb mesh
 282 structure was used to minimize numerical errors resulting from the radial groundwater

283 flow pattern around injection and monitoring wells, and other cases of flow vector
284 orientations deviating significantly from a direction perpendicular to interfaces between
285 model grid blocks.

286 **3.2. Hydrological parameters**

287 Hydrodynamic parameters used in the model are listed in Table 3. Two pumping
288 tests were conducted to measure the hydraulic conductivity. Drawdown data from a 39-
289 hour pumping test were used to calculate an average hydraulic conductivity of 41 ft/day
290 (12.5 m/day or 1.45×10^{-4} m/s) and a storativity of 0.00017 for the transmissive
291 stratigraphic interval in which the test was conducted. Data from another 18-hour
292 pumping test yielded close agreement with a hydraulic conductivity of 47 ft/day (14.3
293 m/day or 1.65×10^{-4} m/s) and a storativity of 0.00029. The hydraulic conductivity used in
294 the model is the average of values from these two pumping tests (13.4 m/day),
295 corresponding to a permeability of 1.55×10^{-11} m². The storativity used in the model was
296 taken as 0.00023, which was converted to a pore compressibility of 3.8×10^{-9} Pa⁻¹
297 assuming zero water expansivity.

298 In TOUGHREACT, hydrodynamic dispersion is not computed. The effect of
299 dispersion is approximated by numerical dispersion, which is roughly equal to half the
300 spacing of grid blocks and in the present case corresponds to dispersivity values between
301 0.25 m close to the injection well and 0.5 m further away.

302

303

Table 3. Hydrodynamic parameters used in the model

Parameter	Aquifer
Porosity ϕ	0.3

Permeability [m ²]	1.55×10 ⁻¹¹
Hydraulic conductivity (m/day)	13.4
Pore compressibility (Pa ⁻¹)	3.8×10 ⁻⁹
Average molecular diffusion coefficient (m ² /s) for all aqueous species	1×10 ⁻⁹
Dispersivity	0.25 m (numerical)
Tortuosity	0.67*

304 * Based on the Millington and Quirk (1961) equation

305

306 **3.3. Geochemical parameters**

307 Table 4 lists the chemical composition of initial (ambient) pore water and injected
308 water in the model. The initial composition of the modeled water was based on average
309 concentrations measured over a 20-month pre-injection baseline period. Detection limits
310 were used for the concentration of species for which concentrations were below the
311 detection limit. The pH and carbonate composition of the injected water were computed
312 by assuming equilibration of the initial water with a partial CO₂ pressure (P_{CO_2}) of 3.8 bar,
313 corresponding to full saturation of the water with CO₂ gas at the prevailing local
314 hydrostatic pressure. The pH value obtained in this manner (4.97) is consistent with
315 measured pH values in the field (~5) after injection started. The injected water has
316 essentially the same composition as the initial water except for its lower pH and higher
317 total dissolved carbonate concentration (0.133 moles/kg). The initial water is slightly

318 under-saturated with respect to calcite, with a saturation index of -0.5; in contrast, the
 319 calcite saturation index in the injected water is much lower (-3.3) due to the lower pH
 320 induced by carbonation.

321

322 Table 4. Composition of initial water used in the model. The unit of concentration of
 323 chemical species is molality (moles per kg water)

Species	Concentration	Species	Concentration	Species	concentration
pH	7.91	K	7.10×10^{-5}	Zn	2.14×10^{-7}
Al	4.45×10^{-6}	Li	6.97×10^{-6}	S(-2)	3.70×10^{-5}
Ba	4.07×10^{-7}	Mg	5.35×10^{-5}	Cr	4.81×10^{-8}
Br	8.27×10^{-7}	Mn	1.16×10^{-6}	Se	7.00×10^{-9}
Ca	7.34×10^{-5}	Mo	4.41×10^{-8}	As	9.22×10^{-9}
Cd	8.45×10^{-10}	Na	6.70×10^{-3}	N(+5)	1.67×10^{-4}
Cl	7.31×10^{-4}	Ni	3.41×10^{-8}	Acetic acid (aq)	5.31×10^{-5}
Co	9.67×10^{-9}	Pb	9.65×10^{-10}	Methane(aq)	9.87×10^{-6}
Cu	1.73×10^{-8}	S(+6)	1.02×10^{-5}	Ethane(aq)	2.51×10^{-5}
F	2.40×10^{-5}	Sb	1.33×10^{-8}	Hg	3.49×10^{-10}
Fe(II)	4.00×10^{-6}	Si	1.75×10^{-4}	Fe(III)	3.46×10^{-6}
C(+4)	6.22×10^{-3}	Sr	1.13×10^{-6}	O ₂ (aq) #	1.08×10^{-74}
P	3.18×10^{-6}	Na	6.70×10^{-3}		

324 # Computed from redox couple HS⁻/SO₄⁻²

325 Chemical reactions considered in the model are aqueous complexation, surface
 326 complexation (using a double diffuse layer model), cation exchange (using the Gaines-
 327 Thomas convention) and mineral precipitation/dissolution under kinetic constraints
 328 (using published rate laws). Aqueous complexes considered in the model are listed in
 329 Table A1 in the Appendix. The cation exchange and surface complexation reactions are
 330 listed in Table A2 and A3 in the Appendix, respectively. In the current geochemical
 331 model, it is assumed that ferrihydrite (as Fe(OH)₃(s)) is the adsorbent. The reaction
 332 constants for surface complexation of H⁺ and chromium are taken from Dzombak and

333 Morel (1990), for surface complexation reactions of iron and carbonate from Appelo et al.
334 (2002), and for surface complexation on silicate from Jordan et al. (2007).

335 Based on the mineralogical characterization of the sediment, the model
336 considered illite, smectite, $\text{Fe}(\text{OH})_3(\text{s})$ and amorphous iron sulfide (mackinawite, FeS_m),
337 in addition to major aquifer minerals such as quartz, K-feldspar and plagioclase (Table 4).
338 The amount of iron sulfide (FeS_m) was estimated from selective extractions (~0.02
339 vol%), and the amount of $\text{Fe}(\text{OH})_3(\text{s})$ from calibration of sediment acid titration
340 simulations (~0.135 vol%) as discussed later. Carbonates were not detected using x-ray
341 diffraction (XRD) and solid total inorganic carbon-total organic carbon (TIC-TOC)
342 analysis. However, calcite was found by micro-X ray spectroscopy (Varadharajan et al.,
343 2013). Therefore, trace amounts of calcite were included in the simulations, with an
344 amount calibrated to yield best agreement between simulated and observed metal
345 concentration trends. The amounts of illite, smectite, quartz, and K-feldspar were roughly
346 estimated based on XRD characterization of sediment cores and thin sections (Table 5).
347 Equilibrium constants for these minerals and other secondary phases allowed to form are
348 given in Table 5. These data, as well as dissociation constants for all considered aqueous
349 species (Table A1) were taken from the *Data0.dat.YMPv4.0* EQ3/6 thermodynamic
350 database (Wolery, 2007; SNL 2007). Details on the implemented rate laws and kinetic
351 data for mineral dissolution are given in Appendix A.

352

353 Table 5. Equilibrium constants ($\log(K)$) and initial volume fraction of minerals
354 in the sediment (on a dry basis). $\log(K)$ values are for dissolution reactions that
355 are written with the primary species listed in the first column of Table A1.

Primary Mineral	Volume fraction (%)	logK(25 °C)	Potential Secondary Minerals allowed to form	logK(25°C, 1 bar)
Quartz	94.4	-3.75	Dolomite	2.52
Calcite	0.0086	1.85	Siderite	-0.25
FeS m	0.01	-3.5	Witherite	1.77
K-feldspar	2	-22.39	Rhodochrosite	0.252
Smectite-Na	0.5	-38.32	Strontianite	-0.31
Illite	1	-42.69	Dawsonite	-17.9
Fe(OH) ₃ (s)	0.135	-5.66		
Ab80An20	2	-14.8		

356

357 **3.4. pH Buffering Capacity**

358 Sediment titrations were conducted to evaluate the pH buffering capacity of the aquifer
359 (Varadharajan et al., 2013). A mixture of 1 g sediment and 5 ml deionized water was
360 titrated with a 0.01M HCl solution. Simulations of these sediment acid titrations were
361 used to constrain pH buffering reactions implemented in the reactive transport model.
362 These reactions were assumed to consist primarily of surface protonation/deprotonation
363 reactions, as well as the dissolution of carbonate minerals (calcite). However, the
364 simulations showed that the calcite amount in the sediments (Table 5) was too small to
365 significantly buffer pH upon acid titration. This implies that, for these sediments, the pH
366 buffering behavior was dominated by H⁺ adsorption. To model such adsorption,
367 protonation/deprotonation reaction equilibrium constants and sorption site densities were
368 taken from Dzombak and Morel (1990), assuming that H⁺ adsorption occurs dominantly
369 onto ferric iron (oxy)hydroxides (here modeled as ferrihydrite in the form of Fe(OH)₃(s)).
370 Using these data, the volume fraction of Fe(OH)₃(s) in the sediment was then calibrated
371 (0.135%) to best reproduce the titration curve obtained for sample PW-1-160 that is

372 representative of the aquifer sandy sediment (Figure A1 in electronic supplementary
373 information (ESI)).

374

375 **4. Modeling results**

376 Results of various simulations are presented below and organized as follows. First, results
377 of a “base case” model are presented. This model implements the metal release reactions
378 postulated in Table 2, with focus on simulated trends of pH, alkalinity, and
379 concentrations of alkali and alkaline earth metals, Ba, Fe, Si and Cr. In a second part, we
380 then evaluate the sensitivity of modeling results to a variety of key parameters and
381 processes such as surface protonation, calcite dissolution, and cation exchange capacity
382 (CEC). Finally, we also explore conceptual model variations to help explain some of the
383 discrepancies between observed metal concentration trends and the base-case model
384 results.

385

386 **4.1. Base-Case Model**

387 *pH and Alkalinity*

388 Groundwater pumped out from PW-1 is saturated with CO₂ at the surface and then
389 injected through IW-1. The dissolved CO₂ dissociates into bicarbonate and protons (CO₂
390 + H₂O ⇌ HCO₃⁻ + H⁺), which increases the total dissolved inorganic carbon content (DIC)
391 and decreases pH in the impacted groundwater. This carbonated water displaces the
392 groundwater in the aquifer, spreads out from IW-1 towards PW-1, and forms a plume of
393 elliptic shape that is high in DIC and low in pH, as illustrated by the simulated spatial
394 distribution of pH at several time points (Figure 6a and b). The center of the plume has a

395 pH of around 5; the edge of the plume a pH between 5 and 8 caused by dispersion and
396 buffering of the acidic plume by chemical reactions. Low-pH groundwater arrives first at
397 MW-3, then at MW-2 and MW-1. At the end of the injection/pumping period (i.e., 156
398 days after the injection and pumping started), low-pH groundwater arrives at MW-4
399 (Figure 6c). Once injection/pumping ends, because of the stagnant regional groundwater
400 flow, the plume remains at the same location, however, the pH value at the center of the
401 plume increases gradually.

402 Modeling results for groundwater pH match measured data reasonably well, but
403 some discrepancies are observed (Figure 6c). For example, the pH at MW-4 started to
404 drop earlier in the model compared to what was observed in the field. Furthermore, at
405 other well locations the modeled pH does not rebound fast enough to match the recovery
406 exhibited in the field. A change in dissolved CO₂ concentration is just one of many
407 processes that can affect groundwater pH. Other processes include the dissolution of
408 calcite and plagioclase, and surface complexation. Sensitivity analyses reported later in
409 this paper illustrate how these processes affect the simulated spatial and temporal
410 evolution of pH.

411 Figure 7a and b show the modeled spatial distribution of alkalinity at two time-points.
412 Given the high-DIC concentrations during injection and the simulated pH conditions of
413 the plume, bicarbonate (HCO₃⁻) is the dominant component of total alkalinity, with much
414 lower concentrations of carbonate (CO₃⁻²). Hence, the simulated alkalinity values are
415 taken as the sum of the predicted concentrations of HCO₃⁻ and CO₃⁻². Unlike the plume of
416 DIC and pH, the plume of bicarbonate is shaped like a donut—higher concentrations at

417 the moving edge of the plume but very low concentration in the center, which is caused
418 by the dominance of carbonic acid (H_2CO_3^0) once the pH drops below about 6.

419 The modeled alkalinity values are compared with the measured total alkalinity trends in
420 Figure 7c. As the plume passes the monitoring wells, the temporal evolution of alkalinity
421 shows a pulse-like shape initially, followed by a slow recovery after CO_2 injection and
422 pumping stopped. This trend is clearly observed at MW-1, MW-2 and MW-3, but less
423 pronounced at MW-4. Computed and measured breakthroughs of alkalinity are similar at
424 MW-3, but only show qualitative and not quantitative agreements at other wells. The
425 major discrepancy between model results and field data is that the computed peak heights
426 of alkalinity breakthrough curves *increase* for wells further away from IW-1, while the
427 observed peak heights *decrease* with longer distances away from IW-1. This type of
428 discrepancy persists for breakthrough curves of most dissolved species, as discussed later.

429 Alkali and alkaline earth metals

430 The increase in carbonate content and the drop of pH trigger the dissolution of
431 two calcium-bearing minerals: calcite and Ab80An20 (a plagioclase with 80% albite and
432 20% anorthite). The former dissolves much faster than the latter. The current model
433 calibration indicates that the amount of calcite is fairly small and would be depleted
434 shortly after the arrival of acidified water. The dissolution of a limited amount of calcite
435 creates a donut-shape plume of Ca as shown in Figure 8a and b. Regarding the
436 breakthrough curves of Ca at the four monitoring wells (Figure 8c), two concentration
437 trends can be observed: (1) a pulse-like temporal change characterized by a rise in Ca
438 concentrations upon the arrival of acidified water followed by a decrease in

439 concentrations until the end of CO₂ injection (“pulse period”), and (2) a bounce-back of
440 Ca concentration levels during the post-injection period (“recovery period”).
441 This evolution of Ca at MW-3 was interpreted by Zheng et al. (2015) with a model
442 concept that encompasses (a) a fast-reacting but limited pool of reactive minerals that
443 respond quickly to changes in pH and can explain the pulse period, and (b) a slow-
444 reacting but essentially unlimited mineral pool to yield rising concentrations upon
445 decreased groundwater velocities after pumping and injection stopped in the recovery
446 period. This conceptualization combines the initial fast pulsing behavior with transport-
447 limited kinetic dissolution trends (e.g., Johnson et al., 1998) that are strongly dependent
448 on groundwater residence times. Under these conditions, rising metal concentrations from
449 the dissolution of minerals are only noticeable when the groundwater velocity is slow
450 (relative to the reaction rate) or inversely when reaction rates are fast (relative to the
451 groundwater velocity). For Ca, the fast-reacting but limited pool is the dissolution of a
452 limited amount of calcite (~0.009% in volume fraction), and the slow-reacting but
453 essentially unlimited pool is the dissolution of plagioclase. The close match between the
454 computed and measured breakthrough curves of Ca at MW-3 support this concept. Model
455 results at other wells, however, fail to quantitatively reproduce the measured data,
456 although qualitatively they exhibit similar trends. Similarly to alkalinity, the most
457 noticeable discrepancy between modeled and measured data is that the computed
458 breakthroughs at the four monitoring well show increasingly higher peaks with distance
459 from the injection well (IW-1), during the “pulse period”, whereas measured
460 breakthroughs at these four monitoring wells show increasingly lower peaks as the plume
461 moves further away from IW-1.

462 The release of Ca into solution triggers a series of cation exchange reactions that lead to
463 the increase in concentrations of major elements such as Na, K, Mg, Mn, and trace
464 elements such as Ba, Sr, and Li. This explains why the concentrations of these elements
465 exhibit trends parallel to Ca (e.g. see Figure 9a for barium as example). Because cation
466 exchange reactions are fast (relative to mineral dissolution), the temporal evolution of
467 concentrations for these elements (Sr, Li, Na, K, Mg and Mn; Figures A2 to A7 in ESI) is
468 quite similar to that of Ca. The best fits of measured data with model results are achieved
469 for Ba, Sr, Li, and Mg, and the matches between measured and computed values are not
470 as good for Na, K and Mn. The deviations between measured and computed
471 concentrations of Ca at wells other than MW-3 are similar to deviations observed for Ba,
472 Sr, Li, Na, K, Mg and Mn.

473 Iron

474 Measured total Fe concentrations (essentially all Fe(II) within the observed pH range)
475 exhibit similar spatial and temporal distributions as Ca. However, for Fe, the fast-reacting
476 (limited) pool is modeled as the desorption of Fe(II) from the surface of Fe(OH)₃(s), and
477 the slow-reacting (unlimited) pool as the dissolution of iron sulfide. This concept leads to
478 a fair fit between measured and computed data at MW-3 (Figure 9b). However, the initial
479 modeled pulse is much narrower than observed, and with a higher peak than the
480 measured data. This discrepancy may be the result of assuming equilibrium surface
481 complexation reactions. Surface complexation reactions are typically quite fast, ranging
482 from days to weeks, such that these reactions can often be treated as an equilibrium
483 process for the simulation of subsurface systems over the long term. However, in the
484 present case, this assumption may yield a Fe pulse at MW-3 that is too short in time

485 (lasting only a few weeks). As soon as the injection/pumping stops, the simulated
486 concentration of Fe increases, which is modeled here with reasonable results (Figure 9b)
487 by the dissolution of iron sulfide. The pH decrease resulting from the introduction of
488 CO₂ in the subsurface could also induce a greater rate of microbial Fe(III) reduction (Kirk,
489 2011; Kirk et al., 2013). This could not be ruled out as another mechanism leading to
490 increased Fe(II) concentrations in groundwater, also it would not be expected to be the
491 cause of the initial short-lived Fe(II) pulse observed in the field. It should also be noted
492 that the modeled and measured Fe breakthrough curves at MW-1, MW-2 and MW-4 only
493 match qualitatively but not quantitatively.

494 Silicon

495 The spatial and temporal evolution of Si (Figure 9c) is similar to that of Ca and Fe.
496 Therefore, in the base case model, release mechanisms similar to those proposed for Ca
497 and Fe are used to explain the behavior of Si: the fast-reacting (limited) pool for Si is
498 driven by Si desorption from Fe(OH)₃(s) surfaces, and the slow-reacting (unlimited) pool
499 is represented by the dissolution of plagioclase (Ab₈₀An₂₀). This concept explains
500 qualitatively the first “pulse period” and the following “recovery period” exhibited in the
501 breakthrough curves of Si at MW-1, MW-2 and MW-3, but results in similar departures
502 as for other species— moving further away from IW-1, the peaks of the computed
503 breakthrough curves at the four monitoring wells keep increasing, in contrast to the
504 measured breakthrough peaks, which continue decreasing.

505 Chromium

506 Cr appears to behave slightly differently from other metals. The breakthrough of Cr at
507 MW-3 is similar to that of other elements, i.e. an initial “pulse period” is followed by a

508 “recovery period” after injection stopped (Figure 9d). But such a trend is not observed for
509 the Cr breakthrough curves at other wells. Cr breakthrough curves at MW-1 and MW-2
510 only show an initial rising and falling, but no further concentration increase during the
511 recovery period. Cr concentrations at MW-4 are below the detection limit. The model
512 that considers desorption of Cr matches somewhat the measured Cr at MW-3 but not the
513 observed behavior at other wells.

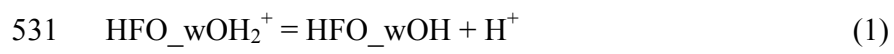
514 **4.2. Sensitivity of model results to input parameters and modeled processes**

515 In this section, we explore the sensitivity of model results to key parameters and reactive
516 processes, trying to shed light on how these processes affect the modeled concentration
517 trends of dissolved major and trace elements as a result of the injection of CO₂-bearing
518 water. These sensitivity analyses are by no means exhaustive and are only intended to
519 show the effect of presumed key input parameters (or particular types of reactions) on
520 model results. To do so, for each sensitivity case, only the model inputs being tested are
521 varied, while the rest of the parameters and reactions remain the same as in the base-case
522 model.

523

524 **4.2.1. The impact of surface complexation on modeled pH**

525 Many reactions can affect groundwater pH, including the pH buffering by the dissolution
526 of calcite (or other carbonate minerals) (e.g. Carroll et al., 2009) and surface protonation
527 reactions (e.g. Zheng et al., 2009; Zheng et al., 2012; Table A3). Another pH-buffering
528 surface reaction that was not considered in these earlier studies is the surface
529 adsorption/desorption of bicarbonate (Appelo et al., 2002). The dominant of these
530 surface complexation reactions can be written as (Table A3):



533

534 In the base-case model, the volume fraction of calcite was found to be too small for
535 calcite to buffer pH significantly. Hence, reactions (1) and (2) are the main reactions that
536 buffer pH. We conducted two sensitivity analyses to illustrate how these two reactions
537 affect the temporal changes of pH: Model “A” does not consider surface complexation of
538 bicarbonate and Model “B” considers neither surface protonation nor surface
539 complexation of bicarbonate. In comparison with the base-case model, Model A leads to
540 an earlier breakthrough of pH, lower pH values, and slightly higher total dissolved
541 carbonate concentrations, with increasingly noticeable differences away from MW-1
542 (Figure 10a and b). Similar but more pronounced differences from the base-case model
543 are predicted if neither surface protonation nor surface complexation of carbonate is
544 considered (Model B) (Figure 10c and d). The earlier breakthrough of pH with models A
545 and B leads to an earlier rise of Ca and trace metals concentrations, which does not fit the
546 measured data as well as the base-case model. It is however noteworthy to mention that
547 these observations are based on specific surface complexation reactions and equilibrium
548 sorption constants (Dzombak and Morel, 1990; Appelo et al., 2002), together with the
549 assumption that $\text{Fe}(\text{OH})_3(\text{s})$ is the dominant adsorbent with an amount calibrated based
550 on sediment titration data (Section 3.4)— Changing any of these model conditions might
551 change the model results described above.

552 **4.2.2. Sensitivity to calcite volume fraction and dissolution rate**

553 In the geochemical model presented here, the calcite dissolution rate and the abundance
554 of calcite play the key role in determining the responses of most major and trace elements,
555 especially during the initial “pulse period” of the breakthrough curve. This is because
556 alkali and alkaline earth metal are released via cation exchange, which is directly driven

557 by the amount of Ca released by calcite dissolution (in other words, increasing the
558 amount of calcite in the model enhances the release of Ca and other metals). In this
559 sensitivity analysis, the calcite effective dissolution rate (r in Equation A1) was
560 increased by raising the specific surface area of calcite by two orders of magnitude.
561 When doing so, the higher calcite dissolution rate has an insignificant impact on pH
562 (Figure A9 in ESI), but leads to a higher peak value and narrower span of the initial Ca
563 concentration pulse (Figure 11a and b). The higher dissolution rate also leads to a faster
564 depletion of calcite. The resulting changes in trace metal (Ba, Mg, Mn, K, Li, Na and Sr)
565 concentrations (see Figure 11b using Ba as an example) follow the Ca trend, because the
566 change in Ca concentration is the driving force for the concentration changes in other
567 trace metals.

568 The current model relies on the dissolution and the subsequent depletion of a limited
569 amount of calcite to explain the pulse-like behavior in the breakthrough of Ca and some
570 major and trace elements. In the base case, the volume fraction of calcite was calibrated
571 yielding a quite a small amount (8.6×10^{-5} , dimensionless units), which is well below
572 XRD detection limits. Figure 11c shows model results for a sensitivity analysis with a
573 calcite volume fraction that is 10 times higher. The higher initial volume fraction of
574 calcite results in a higher Ca concentration peak, a wider span of the pulse, and also in
575 higher Ca concentrations during the recovery period. The concentration profiles of alkali
576 and alkaline earth metals are affected in a similar manner by the increased amount of
577 calcite because their profiles follow that of Ca (see Figure 11d for Ba as an example).
578 The higher initial volume fraction of calcite also leads to a much delayed breakthrough of
579 pH (see Figure A10 in ESI).

580 **4.2.3. Sensitivity to cation exchange capacity (CEC)**

581 The base-case model relies on cation exchange reactions to explain the changes in
582 concentration of Ba, Mg, Mn, K, Li, Na and Sr. Here we vary the CEC value input in the
583 model to examine the effect of CEC on the concentration of relevant species. Figure 12a
584 shows the breakthrough curve of Ca at MW-1 and MW-3 calculated using CEC values
585 that are either twice as large, or half of the value used in the base-case model. Larger
586 CEC values result in more Ca residing in exchangeable sites. . Therefore, the
587 concentration of Ca in the aqueous phase is lower at larger CEC values (Figure 12a).
588 Conversely, it is higher at lower CEC values as less Ca is partitioned on exchangeable
589 sites (Figure 12a). Larger CEC values also mean that exchange sites would retain more
590 trace metals in the solid phase and therefore lead to lower concentration of trace metals in
591 aqueous phase, as exemplified with Ba (Figure 12b).

592 **4.2.4. The Effect of Cation Exchange on Iron Concentrations**

593 In the base case, the desorption of Fe from $\text{Fe}(\text{OH})_3(\text{s})$ surfaces is used to interpret
594 the initial pulse shown in the breakthrough curve of Fe. One question, however, is
595 whether Fe could be rather present in exchangeable surface sites, thus whether cation
596 exchange is rather the process that leads to the increase in Fe concentrations. In order to
597 test this hypothesis, we conducted a simulation (Model C in Figure 13a) in which Fe(II)
598 was included as an exchangeable cation and excluded from sorption sites. With this
599 conceptual model, the release of Fe via cation exchange with Ca is responsible for the
600 initial pulse of Fe. Figure 13a shows the model results of this simulation, using exchange
601 equilibrium constants for Fe(II) from Appelo and Postma (1994). In this case, the

602 computed Fe concentrations are much lower than measured concentrations, therefore
603 suggesting that exchangeable Fe alone does not provide a high enough Fe source.

604

605 **4.3. Enhancing Metal Release Near the Injection Wells**

606 The base-case model and the sensitivity simulations described above assume that
607 the source of trace elements resides in the aquifer, with Ca release by calcite dissolution
608 being the driving force on a series of cation exchange reactions. However, one concept
609 that cannot be completely ruled out is that the top and bottom clay layers bounding the
610 injection interval could be the source of released trace elements. Because the injection
611 well is screened beyond the interval of the sandy aquifer, the injected carbonated water
612 could infiltrate the top and bottom clay layers near the injection well and sweep off some
613 trace elements therein and carry them into the aquifer. Another possibility is simply that
614 the clay content of the aquifer near the injection well could be higher than at other
615 locations due to local heterogeneity. Without resorting to a 3D model, these cases can be
616 tested by either increasing the cation exchange capacity near the injection well, or by
617 increasing the calcite volume fraction in this area, as long as the calcite amount remains
618 low enough to drive more cation exchange (by Ca dissolution) without significantly
619 affecting pH. For simplicity we chose the latter (Model D in Figure 13b), and increased
620 the volume fraction of calcite to 3.5×10^{-4} (dimensionless units) within a 4-meter radius
621 area around the injection well. Note that the total amount of calcite relative the affected
622 area in the aquifer is still too small to have a noticeable effect on the magnitude of pH
623 drop. Because the amount of metals loaded onto exchangeable sites is large enough to
624 account for the observed released concentrations, the amount of exchangeable Ca

625 produced by calcite dissolution is the main factor limiting the release of these metals.
626 Therefore, increasing the volume fraction of calcite near the injection well is equivalent
627 to increasing the source of metals at this location. Figure 13b shows the model results for
628 Ba when applying this concept (similar results for Ca are shown in Figure A11 in ESI).
629 In comparison to the base-case model, this case leads to overall better matches of the
630 measured data at MW-1, MW-2 and MW-4, but to a somewhat worse fit of the data at
631 MW-3. Although this concept leads to slightly worse fit of pH breakthrough (Figure A12
632 in ESI), the overall better match between measured and simulated data for this case
633 suggests that the top and bottom clay formations near the injection well, or a generally
634 increased amount of exchangeable metals at this location (from heterogeneous
635 distribution of clay minerals), could explain the observed decreasing pulse intensity of
636 dissolved metals concentrations away from the injections well.

637 **5. Summary and Conclusions**

638 A controlled release field test was conducted with an extensive water quality
639 monitoring program during and after the injection of carbonated water, to mimic the
640 effect of a potential leak of CO₂ from a deep storage site to a shallow aquifer. This field
641 test provided a great opportunity to evaluate and model potential reactive mechanisms
642 responsible for the release of metals in groundwater and strengthen our understanding of
643 the hydrogeological and chemical processes relevant to potential impacts on groundwater
644 quality at CO₂ geological sequestration sites. Reactive transport models have been
645 developed to interpret the concentration changes observed at four monitoring wells
646 during the field test. The breakthrough curves of major and trace elements at these
647 monitoring wells show a pulse-like change during the carbonated water injection period,

648 followed by slowly increasing concentration levels during the post-injection period. A
649 reasonable match between model results and field data indicate that this trend can be
650 interpreted with a conceptual model that considers (a) a fast-reacting but limited pool of
651 reactive minerals that respond quickly to changes in pH, to explain the pulse-like changes
652 in metal concentrations, and (b) a slow-reacting but essentially unlimited mineral pool
653 that yields rising concentrations upon decreased groundwater velocities after pumping
654 and injection stopped.

655 For Ca, Ba, Mg, Mn, K, Li, Na and Sr, a reasonable agreement of model results with
656 observed data was obtained when the fast-reacting but limited pool was modeled as
657 calcite dissolution and Ca-driven cations exchange reactions, and the slow-reacting but
658 unlimited pool was modeled as the dissolution of plagioclase and longer-term Ca-driven
659 cation exchange. For Fe, best results were obtained when modeling fast desorption from
660 iron hydroxides ($\text{Fe}(\text{OH})_3(\text{s})$) together with slow dissolution of amorphous iron sulfide;
661 similarly, good results for Si were obtained by considering fast desorption of Si from iron
662 hydroxides concomitant with slow dissolution of plagioclase. In our modeling study,
663 small finite amounts of fast-dissolving calcite were assumed to be the source of the initial
664 Ca pulse, although it should be noted that finite amounts of Ca and/or Mg desorbing from
665 organics or hydroxides would be expected to yield a similar pulse behavior.

666 A series of sensitivity analyses demonstrated that the initial calcite volume
667 fraction, calcite dissolution rate and CEC value of the sediments are critical parameters to
668 model the temporal changes in concentrations of Ca, Ba, Mg, Mn, K, Li, Na and Sr. The
669 regional groundwater flow affects not only the time of breakthrough but also the
670 concentration levels during the post-injection period. This is because the groundwater

671 residence time, which is inversely proportional to flow rate, has a direct effect on extent
672 of reaction, thus slow mineral dissolution becomes noticeable only under slow flow rates
673 (large residence times).

674 The most noticeable discrepancy between modeled and observed breakthrough
675 curves is that computed breakthroughs at the four monitoring wells show increasing pulse
676 peak concentrations at wells further away from the injection well (IW-1). In contrast, the
677 observed breakthrough at four monitoring wells show the reverse behavior, with
678 decreasing peak heights of breakthrough curves at larger distances away from IW-1. This
679 discrepancy is reduced when chemical spatial heterogeneity is considered in the model.
680 Essentially, the observed decreasing pulse peaks away from the injection well can be
681 reproduced by modeling a larger initial source of Ca and/or trace elements near the
682 injection well than farther away from it. This source term could result of carbonated water
683 contacting clays (such as the top and bottom aquitards near the injection well), or simply
684 a more abundant fast-release source of Ca (calcite, or possibly Ca-adsorbing organic
685 matter and/or hydroxides) near the injection well. Overall, this study further demonstrates
686 the importance of thorough field geochemical and hydrological characterization for
687 environmental risk assessments, covering both the CO₂ injection and post-injection time-
688 periods at CO₂ sequestration sites, and considering the important effect of groundwater
689 flow rate (residence time) on the magnitude of released metal concentrations.

690 ACKNOWLEDGMENT

691 This work was supported by the Electric Power Research Institute; the EPA, Office of
692 Water, under an Interagency Agreement with the U.S. Department of Energy (DOE) at

693 LBNL, under contract number DE-AC02-05CH11231; and the Assistant Secretary for
694 Fossil Energy, National Energy Technology Laboratory (NETL), National Risk
695 Assessment Program (NRAP), of the US Department of Energy under Contract No.
696 DEAC02-05CH11231.

697

698 **References**

- 699 Appelo, C. J. A. and D. Postma 1994. *Geochemistry, groundwater and pollution*.
700 Rotterdam, Netherlands, A.A.Balkema.
- 701 Appelo CAJ, Van Der Weiden MJJ, Tournassat C, Charlet L. 2002. Surface
702 complexation of ferrous iron and carbonate on ferrihydrite and the mobilization of
703 arsenic. *Environ Sci Technol*. 36(14):3096-103.
- 704 Apps JA, Zheng L, Zhang Y, Xu T, Birkholzer JT. 2010. Evaluation of groundwater
705 quality changes in response to CO₂ leakage from deep geological storage.
706 *Transport in Porous Media*. 82(1):215-46.
- 707 Bacon, D. H., N. P. Qafoku, Z. Dai, E. H. Keating and C. F. Brown 2016. Modeling the
708 impact of carbon dioxide leakage into an unconfined, oxidizing carbonate aquifer.
709 *International Journal of Greenhouse Gas Control* 44: 290-299.
- 710 Cahill AG, Jakobsen R. 2013. Hydro-geochemical impact of CO₂ leakage from
711 geological storage on shallow potable aquifers: A field scale pilot experiment.
712 *International Journal of Greenhouse Gas Control*. (0).

713 Cahill, A. G., P. Marker and R. Jakobsen 2014. Hydrogeochemical and mineralogical
714 effects of sustained CO₂ contamination in a shallow sandy aquifer: A field-scale
715 controlled release experiment. *Water Resources Research* 50(2): 1735-1755.

716 Carroll S, Hao Y, Aines R. 2009. Geochemical detection of carbon dioxide in dilute
717 aquifers. *Geochemical Transactions*. 10(4):1-18.

718 Dafflon, B., Y. Wu, S. S. Hubbard, J. T. Birkholzer, T. M. Daley, J. D. Pugh, J. E.
719 Peterson and R. C. Trautz 2013. Monitoring CO₂ Intrusion and Associated
720 Geochemical Transformations in a Shallow Groundwater System Using Complex
721 Electrical Methods. *Environmental Science & Technology* 47(1): 314-321.

722 Dzombak DA, Morel FMM. 1990. Surface complexation modeling-hydrous ferric oxide.
723 New York: John wiley & sons.

724 Carroll, S., Y. Hao and R. Aines 2009. Geochemical detection of carbon dioxide in dilute
725 aquifers. *Geochemical Transactions* 10(4): 1-18.

726 Harvey, O.R., Qafoku, N.P., Cantrell, K.J., Lee, G., Amonette, J.E., Brown, C.F. 2012.
727 Geochemical implications of gas leakage associated with geologic CO₂ storage, a
728 qualitative review. *Environ. Sci. Technol.* 2013, 47, 23–36.

729 Hou, Z., D. H. Bacon, D. W. Engel, G. Lin, Y. Fang, H. Ren and Z. Fang 2014.
730 Uncertainty analyses of CO₂ plume expansion subsequent to wellbore CO₂
731 leakage into aquifers. *International Journal of Greenhouse Gas Control* 27: 69-80.

732 Humez P, Audigane P, Lions J, Chiaberge C, Bellenfant G. 2011. Modeling of CO₂
733 leakage up through an abandoned well from deep saline aquifer to shallow fresh
734 groundwater. *Transport in Porous Media*. 90(1):153-81.

735 Johnson, J.W., Knauss, K.G., Glassley, W.E., DeLoach, L.D., Tompson A.F.B 1998.
736 Reactive transport modeling of plug-flow reactor experiments: quartz and tuff
737 dissolution at 240°C. *Journal of Hydrology*, 209 (1–4), 81–111.

738 Jordan, N., N. Marmier, C. Lomenech, E. Giffaut and J.-J. Ehrhardt 2007. Sorption of
739 silicates on goethite, hematite, and magnetite: Experiments and modelling.
740 *Journal of Colloid and Interface Science* 312(2): 224-229.

741 Kharaka, Y. K., D. R. Cole, S. D. Hovorka, W. D. Gunter, K. G. Knauss and B. M.
742 Freifeld 2006. Gas-water-rock interaction in Frio Formation following CO₂
743 injection: implications for the storage of greenhouse gases in sedimentary basins.
744 *Geology* 34: 577-580.

745 Kharaka, Y.K., Thordsen, J.J., Hovorka, S.D., Nance, H.S., Cole, D.R., Phelps, T.J.,
746 Knauss, K.G. 2009. Potential environmental issues of CO₂ storage in deep saline
747 aquifers: geochemical results from the Frio-I Brine Pilot test, Texas, USA.
748 *Applied Geochemistry*, 24, 1106–1112.

749 Kharaka, Y.K, Thordsen, J.J., Kakouros, E., Ambats, G., Herkelrath, W.N., Birkholzer,
750 J.T., Apps, J.A., Spycher, N.F., Zheng, L., Trautz, R.C., Rauch, H.W.,
751 Gullickson, K. 2010. Changes in the chemistry of shallow groundwater related to
752 the 2008 injection of CO₂ at the ZERT Field Site, Bozeman, Montana.
753 *Environmental Earth Sciences*, 60 (2), 273–284.

754 Kirk, M.F., Santillan, E.F., Sanford, R.E., Altman, S.J., 2013. CO₂-induced shift in
755 microbial activity affects carbon trapping and water quality in anoxic bioreactors.
756 *Geochimica et Cosmochimica Acta*, 122, 198–208.

757 Kirk, F.E., 2011. Variation in Energy Available to Populations of Subsurface Anaerobes
758 in Response to Geological Carbon Storage. *Environ. Sci. Technol.*, 45, 6676–
759 6682. Kirsch, K., Navarre-Sitchler, A.K., Wunsch, A., McCray, J.E. 2014. Metal
760 release from sandstones under experimentally and numerically simulated CO₂
761 leakage conditions. *Environ. Sci. Technol.* 48, 1436–1442.

762 Lasaga AC, Soler JM, Ganor J, Burch TE, Nagy KL. 1994. Chemical weathering rate
763 laws and global geochemical cycles. *Geochimica et Cosmochimica Acta.*
764 58:2361-8.

765 Lawter, A., N. P. Qafoku, G. Wang, H. Shao and C. F. Brown 2016. Evaluating impacts
766 of CO₂ intrusion into an unconsolidated aquifer: I. Experimental data.
767 *International Journal of Greenhouse Gas Control* 44: 323-333.

768 Lemieux J-M. 2011. Review: The potential impact of underground geological storage of
769 carbon dioxide in deep saline aquifers on shallow groundwater resources.
770 *Hydrogeol J.* 19(4):757-78.

771 Little MG, Jackson RB. 2010. Potential Impacts of Leakage from Deep CO₂
772 Geosequestration on Overlying Freshwater Aquifers. *Environmental Science &*
773 *Technology.* 44(23):9225-32.

774 Lu JM, Partin JW, Hovorka SD, Wong C. 2010. Potential risks to freshwater resources as
775 a result of leakage from CO₂ geological storage: a batch-reaction experiment.
776 *Environ Earth Sci*; 60(2):335-48.

777 Millington, R. J. and J. P. Quirk 1961. Permeability of porous solids. *Transactions of the*
778 *Faraday Society* 57(0): 1200-1207.

779 Numerical Dynamics, 2014. Multibase MS Excel add-in developed by Numerical
780 Dynamics, Inc., 2-3-1 Marunouchi Chiyoda Tokyo
781 Japan. NumericalDynamics.com.

782 McGrath AE, Upson GL, Caldwell MD. 2007. Evaluation and Mitigation of Landfill Gas
783 Impacts on Cadmium Leaching from Native Soils. Ground Water Monitoring &
784 Remediation. 27(4):99-109.

785 Pankow, J. F. and J. J. Morgan 1980. Dissolution of tetragonal ferrous sulfide
786 (mackinawite) in anoxic aqueous systems. 2. Implications for the cycling of iron,
787 sulfur, and trace metals. Environmental Science & Technology 14(2): 183-186.

788 Plummer, L. N., Parkhurst, D. L., Wigley, T. M. L. Critical review of the kinetics of
789 calcite dissolution and precipitation, in Chemical Modeling in aqueous System,
790 Jenne E.; ACS Symposium Series; American Chemical Society: Washington, DC.
791 1979.

792 Palandri J, Kharaka YK. 2004. A compilation of rate parameters of water-mineral
793 interaction kinetics for application to geochemical modeling: US Geol. Surv.
794 Open File report 2004-1068.

795 Peter A, Lamert H, Beyer M, Hornbruch G, Heinrich B, Schulz A, et al. 2012.
796 Investigation of the geochemical impact of CO₂ on shallow groundwater: design
797 and implementation of a CO₂ injection test in Northeast Germany. Environ Earth
798 Sci. 67(2):335-49.

799 Pruess, K., C. Oldenburg and G. Moridis 1999. TOUGH2 User's Guide, Version 2.0,
800 Lawrence Berkeley National Laboratory, Berkeley, CA.

801 Remy N., A. Boucher and J. Wu. 2009, Applied Geostatistics with SGeMS: A User's
802 Guide. New York, Cambridge University Press.

803 Smyth RC, Hovorka SD, Lu J, Romanak KD, Partin JW, Wong C, et al. 2009. Assessing
804 risk to fresh water resources from long term CO₂ injection-laboratory and field
805 studies. Energy Procedia.1(1):1957-64.

806 SNL (2007) Qualification of thermodynamic data for geochemical modeling of mineral-
807 water interactions in dilute systems (data0.ymp.R5), Report ANL-WIS-GS-
808 000003 REV 01. Sandia National Laboratories, Las Vegas, Nevada, ACC:
809 DOC.20070619.0007 (2007).

810 Spangler, L. H., L. M. Dobeck, K. S. Repasky, et al. 2010. A shallow subsurface
811 controlled release facility in Bozeman, Montana, USA, for testing near surface
812 CO₂ detection techniques and transport models. Environmental Earth Sciences
813 60(2): 227-239.

814 Trautz, R. C., J. D. Pugh, C. Varadharajan, L. Zheng, M. Bianchi, P. S. Nico, N. F.
815 Spycher, D. L. Newell, R. A. Esposito, Y. Wu, B. Dafflon, S. S. Hubbard and J. T.
816 Birkholzer 2013. Effect of Dissolved CO₂ on a Shallow Groundwater System: A
817 Controlled Release Field Experiment. Environmental Science & Technology
818 47(1): 298-305.

819 Varadharajan C, Tinnacher C, Pugh J, Trautz RC, Zheng L, Spycher NF, Birkholzer JT,
820 Castillo-Michel H, Esposito RA, Nico PS, 2013. A laboratory study of the initial
821 effects of dissolved carbon dioxide (CO₂) on metal release from shallow
822 sediments, International Greenhouse Gas Control, 19(0): 183-211.

823 Viswanathan H, Dai Z, Lopano C, Keating E, Hakala JA, Scheckel KG, et al. 2012.
824 Developing a robust geochemical and reactive transport model to evaluate
825 possible sources of arsenic at the CO₂ sequestration natural analog site in
826 Chimayo, New Mexico. *International Journal of Greenhouse Gas Control*.
827 10(0):199-214.

828 Wang S, Jaffe PR. 2004. Dissolution of a mineral phase in potable aquifers due to CO₂
829 releases from deep formations; effect of dissolution kinetics. *Energy Conversion*
830 *and Management*.45:2833-48.

831 Wei, Y., M. Maroto-Valer and M. D. Steven 2011. Environmental consequences of
832 potential leaks of CO₂ in soil. *Energy Procedia* 4(0): 3224-3230.

833 Wilkin RT, Digiulio DC. 2010. Geochemical Impacts to Groundwater from Geologic
834 Carbon Sequestration: Controls on pH and Inorganic Carbon Concentrations from
835 Reaction Path and Kinetic Modeling. *Environmental Science & Technology*.
836 44(12):4821-7.

837 Wolery T. and Jove-Colon C., 2007. Qualification of Thermodynamic Data for
838 Geochemical Modeling of Mineral-Water Interactions in Dilute Systems. ANL-
839 WIS-GS-000003 REV 01. Las Vegas, Nevada: Sandia National Laboratories.
840 ACC: DOC.20070619.0007.

841 Wunsch A., Navarre-Sitchler, A.K., Moore, J., McCray, J.E. 2014. Metal release from
842 limestones at high partial-pressures of CO₂. *Chemical Geology* 363, 40–55.

843 Yang, C., P. J. Mickler, R. Reedy, B. R. Scanlon, K. D. Romanak, J.-P. Nicot, S. D.
844 Hovorka, R. H. Trevino and T. Larson 2013. Single-well push–pull test for
845 assessing potential impacts of CO₂ leakage on groundwater quality in a shallow

846 Gulf Coast aquifer in Cranfield, Mississippi. *International Journal of Greenhouse*
847 *Gas Control* 18(0): 375-387.

848 Zheng L, Apps JA, Zhang Y, Xu T, Birkholzer JT. 2009. On mobilization of lead and
849 arsenic in groundwater in response to CO₂ leakage from deep geological storage.
850 *Chemical geology*. 268(3-4):281-97.

851 Zheng L, Apps JA, Spycher N, Birkholzer JT, Kharaka YK, Thordsen J, et al. 2012.
852 Geochemical modeling of changes in shallow groundwater chemistry observed
853 during the MSU-ZERT CO₂ injection experiment. *International Journal of*
854 *Greenhouse Gas Control*. 7(0):202-17.

855 Zheng L, Spycher N, Birkholzer J, Xu T, Apps J, Kharaka Y. 2013. On modeling the
856 potential impacts of CO₂ sequestration on shallow groundwater: Transport of
857 organics and co-injected H₂S by supercritical CO₂ to shallow aquifers.
858 *International Journal of Greenhouse Gas Control*. 14(0):113-27.

859 Zheng, L., N. Spycher, C. Varadharajan, R. M. Tinnacher, J. D. Pugh, M. Bianchi, J.
860 Birkholzer, P. S. Nico and R. C. Trautz 2015. On the mobilization of metals by
861 CO₂ leakage into shallow aquifers: exploring release mechanisms by modeling
862 field and laboratory experiments. *Greenhouse Gases: Science and Technology* (5):
863 1-16.

864 Zheng, L., N. P. Qafoku, A. Lawter, G. Wang, H. Shao and C. F. Brown 2016.
865 Evaluating impacts of CO₂ intrusion into an unconsolidated aquifer: II. Modeling
866 results. *International Journal of Greenhouse Gas Control* 44: 300-309.

867 Zhong, L., K. J. Cantrell, D. H. Bacon and J. Shewell 2014. Transport of organic
868 contaminants mobilized from coal through sandstone overlying a geological

869 carbon sequestration reservoir. *International Journal of Greenhouse Gas Control*
870 21: 158-164.

871 Xu T, Spycher N, Sonnenthal E, Zhang G, Zheng L, Pruess K. 2011. TOUGHREACT
872 Version 2.0: A simulator for subsurface reactive transport under non-isothermal
873 multiphase flow conditions. *Computers & Geosciences*. 37(6):763-74.

874

875

876

877 **Appendix A**

878 Table A1. List of aqueous complexes used in the model and log(K)'s for reactions that

879 are written with the primary species listed the first column

880

Primary species	Aqueous complex	logK(25 °C)	Aqueous complex	logK(25 °C).	Aqueous complex	logK(25 °C).	Aqueous complex	logK(25 °C).
H ⁺	ClO ₂ ⁻	23.107	CaCO ₃ (aq)	7.009	FeOH ⁺²	2.205	Mg ₄ (OH) ₄ ⁺⁴	39.758
H ₂ O	HSO ₅ ⁻	17.29	CaCl ⁺	0.297	FeSO ₄ (aq)	-2.2	MgOH ⁺	11.681
AlO ₂ ⁻	S ₂ O ₃ ⁻²	133.549	CaCl ₂ (aq)	0.654	FeSO ₄ ⁺	-1.917	MgSO ₄ (aq)	-2.22
Ba ⁺²	SO ₃ ⁻²	46.625	CaHCO ₃ ⁺	-1.043	H ₂ O ₂ (aq)	16.626	Mn ₂ (OH) ³⁺	23.9
Ca ⁺²	Al(SO ₄) ₂ ⁻	-27.104	CaOH ⁺	12.834	H ₂ SO ₄ (aq)	1.021	MnCl ⁺	0.143
Cl ⁻	Al ₁₃ O ₄ (OH) ₂₄	-189.919	CaSO ₄ (aq)	-2.1	H ₂ Se(aq)	-3.807	MnCl ₃ ⁻	0.772
Fe ⁺²	Fe ₁₃ O ₄ (OH) ₂₄	58.85	Fe(CO ₃) ₂ ⁻²	13.498	HAlO ₂ (aq)	-6.596	MnHCO ₃ ⁺	-0.442
HCO ₃ ⁻	Al ₂ (OH) ₂ ⁺⁴	-36.717	Fe(OH) ₃ ⁻	31	HFeO ₂ (aq)	12.021	MnO(aq)	22.203
K ⁺	Al ₃ (OH) ₄ ⁺⁵	-52.731	Fe(OH) ₄ ⁻²	46	HFeO ₂ ⁻	29.202	MnO ₂ ⁻²	48.28
Li ⁺	Al ₂ (OH) ₂ CO ₃ ⁺	-38.721	Fe(SO ₄) ₂ ⁻	-3.214	HMnO ₂ ⁻	34.796	MnO ₄ ⁻	20.219
Mg ⁺²	Al ₃ (OH) ₄ HCO ₃	-58.025	Fe ₂ (OH) ₂ ⁺⁴	2.95	HS ₂ O ₃ ⁻	131.867	MnOH ⁺	10.62
Mn ⁺²	Fe ₂ (OH) ₂ CO ₃ ⁺	0.627	Fe ₃ (OH) ₄ ⁺⁵	6.3	HSO ₄ ⁻	-1.975	MnSO ₄ (aq)	-1.903
Na ⁺	Fe ₃ (OH) ₄ HCO ₃	0.986	FeCO ₃ (aq)	4.879	KCl(aq)	2.541	NaCO ₃ ⁻	9.814
SO ₄ ⁻²	AlO ⁺	-11.857	FeCl ⁺	0.165	KHSO ₄ (aq)	1.502	NaCl(aq)	0.782
SiO ₂ (aq)	Al ⁺³	-22.199	FeCl ⁺²	-1.475	KOH(aq)	14.44	NaHCO ₃ (aq)	-0.149
Sr ⁺²	AlOH ⁺²	-17.2	AlCl ⁺²	-21.685	KSO ₄ ⁻	-0.875	NaOH(aq)	14.206
Zn ⁺²	AlSO ₄ ⁺	-25.214	FeCl ₂ (aq)	8.181	LiCl(aq)	1.517	NaSO ₄ ⁻	-0.696
HS ⁻	BaCO ₃ (aq)	7.691	FeHCO ₃ ⁺	-1.47	LiOH(aq)	13.65	OH ⁻	13.991
Fe ⁺³	BaCl ⁺	0.503	FeO(aq)	20.412	LiSO ₄ ⁻	-0.77	SrCO ₃ (aq)	7.47
O ₂ (aq)	BaHCO ₃ ⁺	-1.012	MgO(aq)	24.491	MgCO ₃ (aq)	7.356	SrCl ⁺	0.253
	BaOH ⁺	13.502	CaO(aq)	24.851	MgCl ⁺	0.139	SrHCO ₃ ⁺	-1.226
	CO ₂ (aq)	-6.341	FeO ⁺	5.652	MgHCO ₃ ⁺	-1.033	SrOH ⁺	13.303
	CO ₃ ⁻²	10.325	FeO ₂ ⁻	21.618	FeOH ⁺	9.315	SrSO ₄ (aq)	-2.3

881

882 Table A2. Cation exchange reactions and selectivity coefficients, using the Gaines-
 883 Thomas convention (Appelo and Postma, 1994)

Cation exchange reaction	$K_{Na/M}$
$Na^+ + X-H = X-Na + H^+$	1
$Na^+ + X-K = X-Na + K^+$	0.2
$Na^+ + 0.5X-Ca = X-Na + 0.5Ca^{+2}$	0.4
$Na^+ + 0.5X-Mg = X-Na + 0.5Mg^{+2}$	0.45
$Na^+ + 0.5X-Ba = X-Na + 0.5Ba^{+2}$	0.35
$Na^+ + 0.5X-Mn = X-Na + 0.5Mn^{+2}$	0.55
$Na^+ + 0.5X-Sr = X-Na + 0.5Sr^{+2}$	0.35
$Na^+ + X-Li = X-Li + Li^+$	1.1

884
 885 Table A3. Surface complexation reactions and surface complexation constants (logK) on
 886 ferrihydrite (double diffuse layer model) (Dzomback and Morel, 1990; Appelo et al.,
 887 2002; Jordan et al., 2007)

Surface complexation	logK
$HFO_sOH_2^+ = HFO_sOH + H^+$	-7.29
$HFO_wOH_2^+ = HFO_wOH + H^+$	-7.29
$HFO_sO^- + H^+ = HFO_sOH$	8.93
$HFO_wO^- + H^+ = HFO_wOH$	8.93
$HFO_sOFe^+ + H_+ = HFO_sOH + Fe^{+2}$	0.95
$HFO_wOFe^+ + H^+ = HFO_wOH + Fe^{+2}$	2.98
$HFO_wOFeOH + 2H^+ = HFO_wOH + Fe^{+2} + H_2O$	11.55
$HFO_wCO_2^- + H_2O = HFO_sOH + HCO_3^-$	-2.45
$HFO_wCO_2H + H_2O = HFO_sOH + HCO_3^- + H^+$	-10.4
$HFO_sH_3SiO_4 + 3H_2O = HFO_sOH + SiO_2(aq)$	-2.75
$HFO_sH_2SiO_4^- + 3H_2O + H^+ = HFO_sOH + SiO_2(aq)$	1.4



888

889

890 A general form of rate law is implemented for the dissolution and precipitation of solid
891 phases (Lasaga et al., 1994):

892

$$r = kA \left| 1 - \left(\frac{K}{Q} \right)^\theta \right|^\eta \quad (\text{A1})$$

893

894 where r is the kinetic rate, k is the rate constant ($\text{mol}/\text{m}^2/\text{s}$) which is temperature
895 dependent, A is the reactive surface area per kg water, K is the equilibrium constant for
896 the mineral–water reaction written for the dissolution of one mole of mineral, and Q is
897 the ion activity product of the dissolution reaction. Here, for simplicity, the exponents θ
898 and η are assumed to be equal to 1. A is a function of the mineral specific surface area
899 (e.g., cm^2/g mineral), the volume fraction and density of each mineral in the sediment,
900 and porosity.

901 The rate constant for calcite dissolution is given as a combination of neutral, acid and
902 carbonate mechanisms (Plummer and Parkhurst, 1979):

903

$$k_c = 1.5 \times 10^{-6} e^{-E_a^{nu}/RT} + 0.5 e^{-E_a^H/RT} a_H + 9.6 \times 10^{-5} e^{-E_a^{CO2}/RT} a_{CO2} \quad (\text{A2})$$

904

905 where E_a^{nu} , E_a^H and E_a^{CO2} are activation energies with values of 23.5, 14.4 and 35.4
 906 (kJ/mol), respectively. The rate constant for the neutral, acid and carbonate mechanisms,
 907 are respectively 1.5×10^{-6} , 0.5 and 9.6×10^{-5} . a_H is the H^+ activity and a_{CO2} is the activity
 908 of dissolved CO_2 . In the model, the specific surface area of calcite ($9.8 \text{ cm}^2/\text{g}$) was
 909 calibrated, together with the initial calcite volume fraction, to match the breakthrough of
 910 observed alkaline earth metals concentrations of Ca, Ba and Sr in MW-3. Assuming
 911 spherical grains, the value of the calibrated surface area would correspond to the
 912 geometric surface area of millimeter-sized grains. Because the product of the specific
 913 surface area and volume fraction is of relevance to the reaction rate (not each value
 914 individually), calibrated values of specific surface area or volume fraction should be
 915 viewed as non-unique (co-linearly varying) values.

916 The specific surface areas and kinetic rates of minerals other than calcite are listed in
 917 Table A4. Most rate constants were taken from Palandri and Kharaka (2004). The
 918 dissolution rate constant of plagioclase (Ab80An20) was calibrated based on Ca
 919 concentration changes observed at MW-3. The rate constant is higher than that of albite
 920 but lower than that of anorthite (Palandri and Kharaka, 2004). The rate constant for
 921 FeS_m was taken from Pankow and Morgan (1980). Specific surface areas for most
 922 minerals were arbitrarily set to the same value as for calcite, except for FeS_m, for which
 923 the surface area was increased ($56 \text{ cm}^2/\text{g}$) to match Fe concentrations at MW-3.

924

925 Table A4. Kinetic properties for minerals considered in the model (see text for sources)

Mineral	A	Parameters for Kinetic Rate Law
---------	---	---------------------------------

	(cm ² /g)	Neutral Mechanism		Acid Mechanism			Base Mechanism		
		k ₂₅ (mol/m ² /s)	E _a (KJ/mol)	k ₂₅	E _a	n(H ⁺)	k ₂₅	E _a	n(H ⁺)
Primary:									
Quartz	9.8	1.023×10 ⁻¹⁴	87.7						
K-feldspar	9.8	3.89×10 ⁻¹³	38	8.71×10 ⁻¹¹	51.7	0.5	6.31×10 ⁻¹²	94.1	-0.823
Ab80An20	9.8	1.95×10 ⁻¹²	65	2.95×10 ⁻⁴	69.8	0.457			
Kaolinite	9.8	6.91×10 ⁻¹⁴	22.2	4.89×10 ⁻¹²	65.9	0.777	8.91×10 ⁻¹⁸	17.9	-0.472
Smectite-Ca	9.8	1.66×10 ⁻¹³	35	1.05×10 ⁻¹¹	23.6	0.34	3.02×10 ⁻¹⁷	58.9	-0.4
Illite	9.8	1.66×10 ⁻¹³	35	1.05×10 ⁻¹¹	23.6	0.34	3.02×10 ⁻¹⁷	58.9	-0.4
Fe(OH) ₃ (s)	9.8	2.51×10 ⁻¹⁵	66.2	8.7×10 ⁻¹¹	66.2	1.0			
FeS _m	56.0	3.27×10 ⁻⁷	0						
Secondary:									
Gypsum	9.8	1.62×10 ⁻³	0						
Dolomite	9.8	2.51×10 ⁻⁹	95.3	1.74×10 ⁻⁴	56.7	0.5			
Siderite	9.8	2.51×10 ⁻⁹	95.3	1.74×10 ⁻⁴	56.7	0.5			
Witherite	9.8	2.51×10 ⁻⁹	95.3	1.74×10 ⁻⁴	56.7	0.5			
Rhodochrosite	9.8	2.51×10 ⁻⁹	95.3	1.74×10 ⁻⁴	56.7	0.5			
Strontianite	9.8	2.51×10 ⁻⁹	95.3	1.74×10 ⁻⁴	56.7	0.5			
Dawsonite	9.8	1×10 ⁻⁷	62.8						

